



Copper-catalysed exclusive CO₂ to pure formic acid conversion via single-atom alloying

Tingting Zheng^{1,2,3,7}, Chunxiao Liu^{1,3,7}, Chenxi Guo^{4,7}, Menglu Zhang³, Xu Li³, Qiu Jiang¹, Weiqing Xue³, Hongliang Li³, Aowen Li⁵, Chih-Wen Pao⁶, Jianping Xiao^{1,4}✉, Chuan Xia^{1,2}✉ and Jie Zeng³✉

Converting CO₂ emissions, powered by renewable electricity, to produce fuels and chemicals provides an elegant route towards a carbon-neutral energy cycle. Progress in the understanding and synthesis of Cu catalysts has spurred the explosive development of electrochemical CO₂ reduction (CO₂RR) technology to produce hydrocarbons and oxygenates; however, Cu, as the predominant catalyst, often exhibits limited selectivity and activity towards a specific product, leading to low productivity and substantial post-reaction purification. Here, we present a single-atom Pb-alloyed Cu catalyst (Pb₁Cu) that can exclusively (~96% Faradaic efficiency) convert CO₂ into formate with high activity in excess of 1 A cm⁻². The Pb₁Cu electrocatalyst converts CO₂ into formate on the modulated Cu sites rather than on the isolated Pb. In situ spectroscopic evidence and theoretical calculations revealed that the activated Cu sites of the Pb₁Cu catalyst regulate the first protonation step of the CO₂RR and divert the CO₂RR towards a HCOO* path rather than a COOH* path, thus thwarting the possibility of other products. We further showcase the continuous production of a pure formic acid solution at 100 mA cm⁻² over 180 h using a solid electrolyte reactor and Pb₁Cu.

CO₂ electrolysis to liquid fuels using renewable energy provides an elegant route to offset the extra carbon footprint^{1–5}. Among the diversified products from electrochemical CO₂ reduction (CO₂RR), formic acid (HCOOH) fuel shows the highest profit per mole of electrons⁶. HCOOH itself has a very high energy density, and is being widely explored as a hydrogen storage material and chemical fuel for fuel cells⁷. Up to now, the reported HCOOH-selective electrocatalysts, such as Bi, Sn, In, Pb and Pd, unfortunately have all failed in either activity (<500 mA cm⁻²) or stability (<20 h)^{8–12}, impeding the practical application of CO₂RR. Cu has been regarded as the most promising CO₂RR catalyst and has the advantages of high activity, ease of processing and low cost^{13–18}. However, selective formate production from CO₂RR using Cu catalysts is generally very difficult due to the barely precluded C–C coupling process, and only a few studies have achieved reasonable selectivity (>80% Faradaic efficiency, FE)^{19,20}. In general, CO₂ molecules first undergo adsorption and activation through their interaction with atoms on the catalyst surface, followed by the formation of HCOO* or COOH* intermediates^{21,22}. The former determines the production of formate, whereas the latter (and its subsequent CO*/CO–CO* derivatives) produces other C₁ and C₂₊ products beyond formate^{23,24}. Once the reaction over Cu has been directed towards the HCOO* path, Cu-based catalysts offer great potential for the long-term commercial conversion of CO₂ into HCOOH.

Single-atom alloys (SAAs), which consist of foreign atoms diluted in the matrix of a host metal, possess peculiar electronic and geometric features that are rather different from their constituent

metals. These unique features can endow SAA catalysts with distinct reaction pathways^{25,26}. For instance, Pt₁Cu single-atom alloys showing the interfacial synergy effect change the reaction pathway of glycerol hydrogenolysis from dehydrogenation to dehydration²⁶. Inspired by single-atom alloying chemistry, we sought to explore a single-atom alloyed Cu catalyst for the CO₂-to-formate conversion. We exploited the fact that the suppression of the oxygen protonation of CO₂ to intermediate COOH* promotes formate production, and hence the fact that precise electronic/geometric tuning using isolated heteroatoms on an active metal catalyst promotes the carbon protonation of CO₂ and increases the reaction barrier of competitive hydrogen evolution. We anticipated that the intrinsic properties of the Cu catalyst can be modulated, by alloying with other isolated metal atoms, in a manner that prefers HCOO* to COOH* adsorption and thus favours formate evolution (Fig. 1a).

Results and analysis

Here, we report a Pb single-atom alloyed Cu catalyst (Pb₁Cu) to realize near unity selectivity of formate with record activity. We synthesized the Cu–Pb precursor using an epoxide gelation approach (see Methods), which yielded nanohybrid structures comprising Cu₂(OH)₃Cl and PbCl₂ (Supplementary Figs. 1 and 2). To form the Pb₁Cu SAA catalyst, the as-prepared Cu–Pb precursor was electrochemically reduced in situ under a constant current density of –500 mA cm⁻² in CO₂-saturated 0.5 M KHCO₃ electrolyte for 30 min (see Methods). The powder X-ray diffraction pattern of the as-synthesized Cu–Pb catalyst indicated a pure Cu₂O crystal

¹School of Materials and Energy, University of Electronic Science and Technology of China, Chengdu, People's Republic of China. ²Yangtze Delta Region Institute (Huzhou), University of Electronic Science and Technology of China, Huzhou, People's Republic of China. ³Hefei National Laboratory for Physical Sciences at the Microscale, Key Laboratory of Strongly Coupled Quantum Matter Physics of Chinese Academy of Sciences, National Synchrotron Radiation Laboratory, Key Laboratory of Surface and Interface Chemistry and Energy Catalysis of Anhui Higher Education Institutes, Department of Chemical Physics, University of Science and Technology of China, Hefei, People's Republic of China. ⁴State Key Laboratory of Catalysis, Dalian Institute of Chemical Physics, Chinese Academy of Sciences, University of Chinese Academy of Sciences, Dalian National Laboratory for Clean Energy, Dalian, People's Republic of China. ⁵School of Physical Sciences and CAS Key Laboratory of Vacuum Physics, University of Chinese Academy of Sciences, Beijing, People's Republic of China. ⁶National Synchrotron Radiation Research Center, Hsinchu, Taiwan. ⁷These authors contributed equally: Tingting Zheng, Chunxiao Liu, Chenxi Guo. ✉e-mail: xiao@dicp.ac.cn; chuan.xia@uestc.edu.cn; zengj@ustc.edu.cn

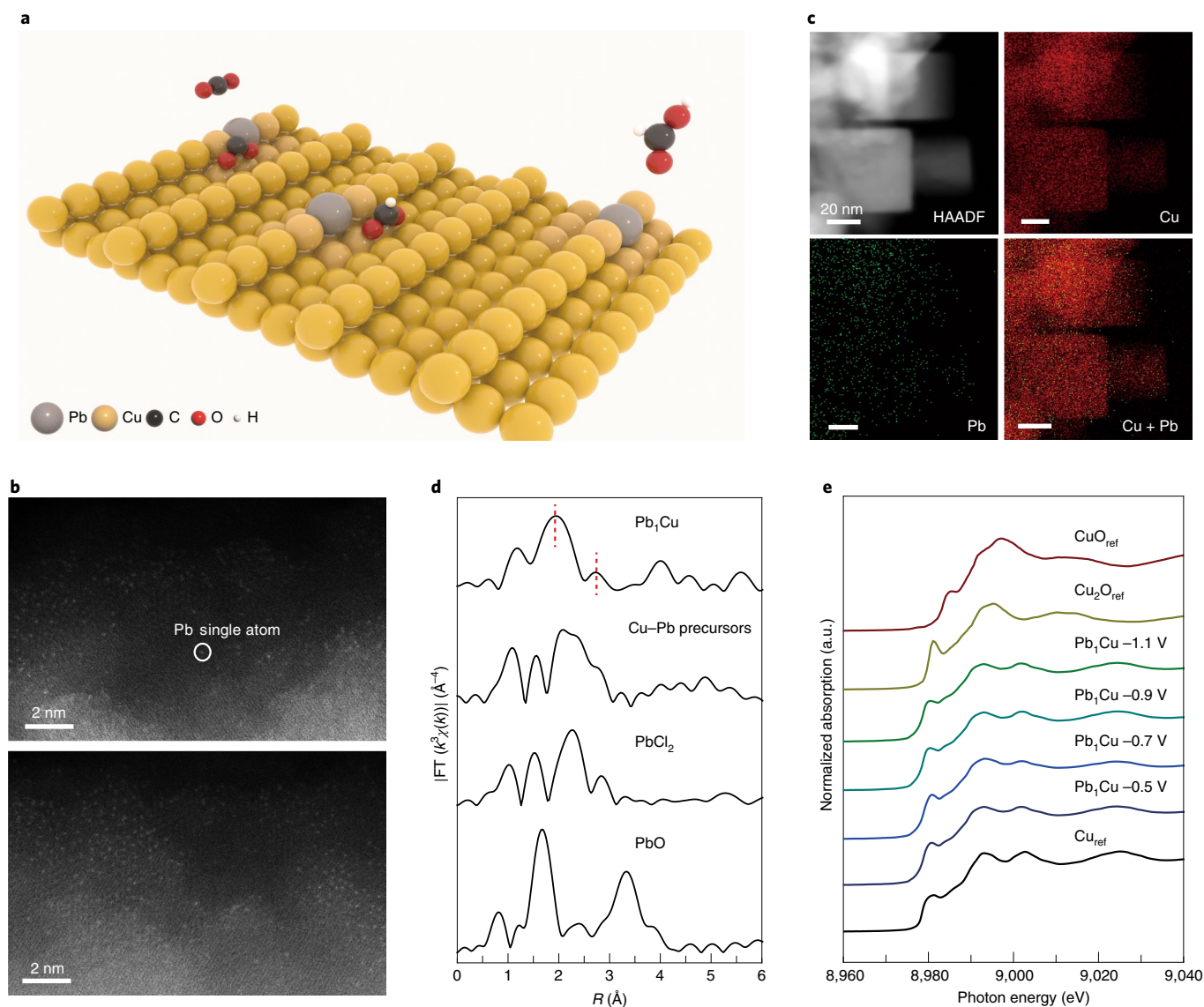


Fig. 1 | Structural characterization of the Pb_1Cu catalyst. **a**, Schematic illustration of CO_2 conversion into HCOOH over a Pb_1Cu SAA. **b**, HAADF-STEM images of the Pb_1Cu catalyst. The white circle highlights the single-dispersed Pb atom. **c**, STEM-EDS mapping of the Pb_1Cu catalyst, showing the atomic dispersion of Pb in the Cu matrix. **d**, Ex situ EXAFS spectra at the Pb L_3 -edge of the Pb_1Cu catalyst. The spectra of PbCl_2 and PbO are shown as references. **e**, In situ XAS spectra at the Cu K-edge of the Pb_1Cu catalyst under formate evolution conditions, along with the spectra of CuO , Cu_2O and Cu as references.

structure (PDF 78-2076, Supplementary Fig. 3), excluding the formation of Pb nanoparticles. Transmission electron microscopy (TEM) images revealed that the in situ generated Cu–Pb catalyst has a cubic morphology with edge lengths ranging from 20 to 50 nm with high homogeneity (Supplementary Fig. 4). The atomic structure of the in situ formed Cu–Pb catalyst was then investigated by high-angle annular dark-field scanning transmission electron microscopy (HAADF-STEM) combined with energy-dispersive X-ray spectroscopy (EDS). Figure 1b clearly indicates the atomic dispersion of Pb atoms in the Cu matrix and the absence of Pb clusters or nanoparticles, suggesting the successful formation of the Pb_1Cu catalyst (Supplementary Fig. 5). This was also confirmed by scanning transmission electron microscopy energy-dispersive X-ray spectroscopy (STEM-EDS) analysis (Fig. 1c). Further large-scale EDS mapping also precluded the existence of Pb particles (Supplementary Fig. 6). The mass loading of Pb in the as-formed Pb_1Cu system was determined to be 4.4 wt% using inductively coupled plasma atomic emission spectroscopy (ICP-AES).

To further investigate the coordination environment of the Pb atoms in the Pb_1Cu catalyst, we performed extended X-ray absorption fine structure (EXAFS) measurements. As shown in Fig. 1d, the EXAFS curve of the Cu–Pb precursor shows a peak at around 2.67 Å attributed to Pb–Cl bonds, whereas Pb_1Cu exhibits two peaks at around 1.93 and 2.73 Å attributed to Pb–O and Pb–Cu bonds²⁷, respectively, verifying the presence of solely atomically dispersed Pb atoms. Note that no Pb–Pb bonds were detected, and the Pb–O bond might be due to the oxidation of the Pb_1Cu catalyst during ex situ tests (Supplementary Fig. 7). Wavelet transform analysis further corroborated the EXAFS fitting results (Supplementary Fig. 8 and Supplementary Table 1). In an effort to elucidate the electronic structure of the Pb_1Cu catalyst under reaction conditions, we conducted an in situ X-ray absorption spectroscopy (XAS) study. The Pb_1Cu catalyst was prepared in situ by reduction of the Cu–Pb precursor in a home-made XAS flow cell at different voltages. Figure 1e shows the Cu K-edge normalized absorption spectra of the in situ formed Pb_1Cu catalyst at different applied potentials, as well as the

spectra of Cu foil, CuO and Cu₂O as controls. The results indicate that the Cu matrix of the Pb₁Cu catalyst exhibit a metallic nature under formate evolution conditions. Unfortunately, we failed to detect Pb signals in situ, probably due to the strong background interference caused by the fluorescence of Cu. The above results, taken together, suggest that the active phase of our in situ formed catalyst under CO₂RR conditions is metallic Cu alloyed with Pb single atoms, namely the Pb₁Cu SAA catalyst.

We next evaluated the CO₂RR catalytic activity of the in situ formed Pb₁Cu catalyst in a standard three-electrode flow cell system using 0.5 M KHCO₃ as the electrolyte (see Methods). Gas and liquid products were separately analysed using gas chromatography (GC) and nuclear magnetic resonance (NMR) spectroscopy, respectively. Linear sweep voltammetry of Pb₁Cu showed a much higher current density in the CO₂-saturated electrolyte than under N₂ atmosphere (Supplementary Fig. 9), indicating the participation of CO₂ gas in the reaction. We found that formate was the only liquid product obtained with Pb₁Cu during CO₂RR, together with a small amount of H₂ and negligible CO (<0.5% FE). The maximal formate FE reached about 96% with a partial current density (j_{formate}) of -800 mA cm^{-2} at about -0.80 V versus the reversible hydrogen electrode (RHE; Fig. 2a and Supplementary Table 2). A high plateau of formate FEs over 90% was retained across a broad potential range from -0.7 to -1.0 V versus RHE, and the competitive hydrogen evolution reaction (HER) was suppressed to below 7%. Notably, at about -1.0 V versus RHE, Pb₁Cu reached a high j_{formate} in excess of $-1,000 \text{ mA cm}^{-2}$, while still maintaining a formate selectivity of 92% (Fig. 2b), outperforming the previously reported formate-selective electrocatalysts (Supplementary Fig. 10). High formate FEs (>80%) were still maintained when the current density was further increased, up to a partial current density of $-1,200 \text{ mA cm}^{-2}$. The long-term stability of the Pb₁Cu catalyst under a conversion rate of -500 mA cm^{-2} was demonstrated in a flow reactor for more than 20 h, with an average formate FE of around 90% (Fig. 2c and Supplementary Fig. 11). Of note, post-catalysis analysis confirmed the fully isolated dispersion of Pb atoms among the Cu of Pb₁Cu (Supplementary Figs. 12–14), suggesting the robustness of the Pb₁Cu coordination structure during CO₂RR. We also transferred the in situ formed Pb₁Cu catalyst to an H-cell with 0.5 M KHCO₃ as the electrolyte, and the catalyst still exhibited an excellent performance with a selectivity of 95.7% towards formate at -0.72 V versus RHE, ranking among the best catalyst performances in an H-cell (Supplementary Fig. 15 and Supplementary Table 3).

Because CO₂RR over the Pb₁Cu catalyst was conducted in 0.5 M KHCO₃ electrolyte, the formate product was generated as a mixture with the dissolved salts, requiring energy-intensive downstream separation. To directly generate pure HCOOH, we sought to transfer the in situ formed Pb₁Cu catalyst to a 3-cm² electrode device with a proton-conducting solid electrolyte (Supplementary Fig. 16)^{28–30} to avoid the mixing of electrolyte and liquid products. In this system, during the selective reduction of CO₂ by the Pb₁Cu catalyst, the generated negatively charged HCOO[−], driven by the electrical field, travels into the middle solid-electrolyte channel. Simultaneously, protons (H⁺) generated by water oxidation on the anode side move into the electrolyte layer to compensate the charge. The electrochemically generated H⁺ and HCOO[−] combine to yield HCOOH, which diffuses away through the liquid water. Under a releasing deionized water flow rate of 45 ml h^{-1} , we observed that the formic acid selectivity remained at >90% across almost the entire cell voltage range (Fig. 2d and Supplementary Fig. 17). A peak HCOOH FE of ~94% with a partial current of -375 mA was achieved at around -3.86 V , corresponding to a 0.16 M pure HCOOH solution. More excitingly, our device can continuously run for 180 h at -3.45 V with negligible performance decay ($\text{FE}_{\text{HCOOH}} > 85\%$, $j_{\text{total}} \approx -100 \text{ mA cm}^{-2}$), resulting in a total of ~81 of 0.1 M pure HCOOH product (Fig. 2e),

which is superior to our previously reported solid electrolyzers (Supplementary Table 4)^{28,30}. ¹H and ¹³C NMR analyses revealed the high purity of the as-obtained HCOOH solution (Supplementary Fig. 18). Taken together, the highly active and selective Pb₁Cu offers the prospect of commercial production of formate from CO₂ and electricity.

We performed a detailed experimental analysis to investigate the possible mechanism for this shift of the CO₂RR pathway away from multiple products to a single HCOOH product over this Cu-based catalyst. First, we prepared a series of samples with varying Pb contents and compared their performances. Combined with their HAADF-STEM images, we inferred that isolated Pb atoms play an important role in the selective generation of formate (Supplementary Fig. 19). To directly link the exclusive selectivity for HCOOH to the impact of alloyed Pb single atoms in the Pb₁Cu catalyst, in a first control experiment we prepared pure Cu nanoparticles by a similar approach to that used for Pb₁Cu for comparison, in a second experiment, we compared Pb₁Cu with a pure Pb nanocatalyst, and in a third experiment we synthesized a Cu catalyst loaded with Pb nanoparticles (Pb@Cu; Supplementary Figs. 20 and 21). The three control catalysts demonstrated much lower performances for the electrochemical CO₂-to-HCOOH conversion than the Pb₁Cu system (Fig. 3a) and generated a mixture of products. These comparisons highlight the critical role of the alloyed single Pb atoms in Pb₁Cu. Second, we conducted in situ electrochemical attenuated total reflection Fourier-transform infrared (ATR-FTIR) spectroscopy to monitor the CO₂RR process on the different catalysts. On scanning the applied potential from -0.5 to -1.3 V versus RHE over the in situ formed pure Cu catalyst, two infrared bands appeared at 1,947 and 2,050 cm^{−1} (Fig. 3c), which we ascribed to surface-bonded CO on Cu derived from COOH* intermediates^{31,32}. *CO is the key intermediate that has been proposed for C–C coupling towards C₂₊ or further hydrogenation towards other C₁ products such as CH₄ (refs. ^{24,33,34}). In stark contrast, no infrared bands for CO over the Pb₁Cu catalyst were observed across the entire potential range (Fig. 3b), showing good agreement with the results of the in situ Raman analysis (Fig. 3e). This result implies the substantial protonation of the carbon in CO₂ instead of oxygen protonation. In addition, the fingerprint infrared band of HCOO[−] was clearly detected at 1,384 cm^{−1} over the Pb₁Cu catalyst³⁵. The band intensities increased on scanning to more negative potentials, which is consistent with the trend of formate formation rates. Intriguingly, we observed that the infrared band corresponding to HCOO[−] appeared at 1,382 and 1,414 cm^{−1} over the pure Cu and Pb metal catalysts (Fig. 3c,d), respectively, whereas a broad infrared band for HCOO[−] with two peaks at 1,393 and 1,412 cm^{−1} was detected over the Pb@Cu catalyst (Supplementary Fig. 22). These observations suggest that the formate intermediates are more likely to be adsorbed on Cu sites rather than on the isolated Pb sites in the Pb₁Cu catalyst (HCOO[−] at 1,384 cm^{−1}). To further support this speculation, we electrodeposited a layer of Cu with a thickness of less than 1 nm or more than 5 nm, respectively, on the as-formed Pb₁Cu catalyst (Supplementary Figs. 23 and 24). We found that Pb₁Cu with an ultrathin Cu layer still produced formate as the exclusive product from CO₂RR, whereas Pb₁Cu with a thick Cu layer generated multiple C₁ and C₂ products. In light of these findings, we speculate that the isolated Pb atoms in the Pb₁Cu SAAs are not intrinsically the active site, but more likely behave as a modifier to finely tune the local geometric/electronic structure of the neighbouring Cu sites, which was further confirmed by theoretical simulation, as will be discussed later, making them highly selective and active for formate evolution.

To simply test our assumption, we introduced other isolated modifier atoms into the Cu catalyst using a similar approach (Supplementary Figs. 25–31). The as-synthesized Bi₁Cu catalyst also showed much improved performance for CO₂-to-formate conversion. To be specific, it delivered a maximum formate FE of 96% at

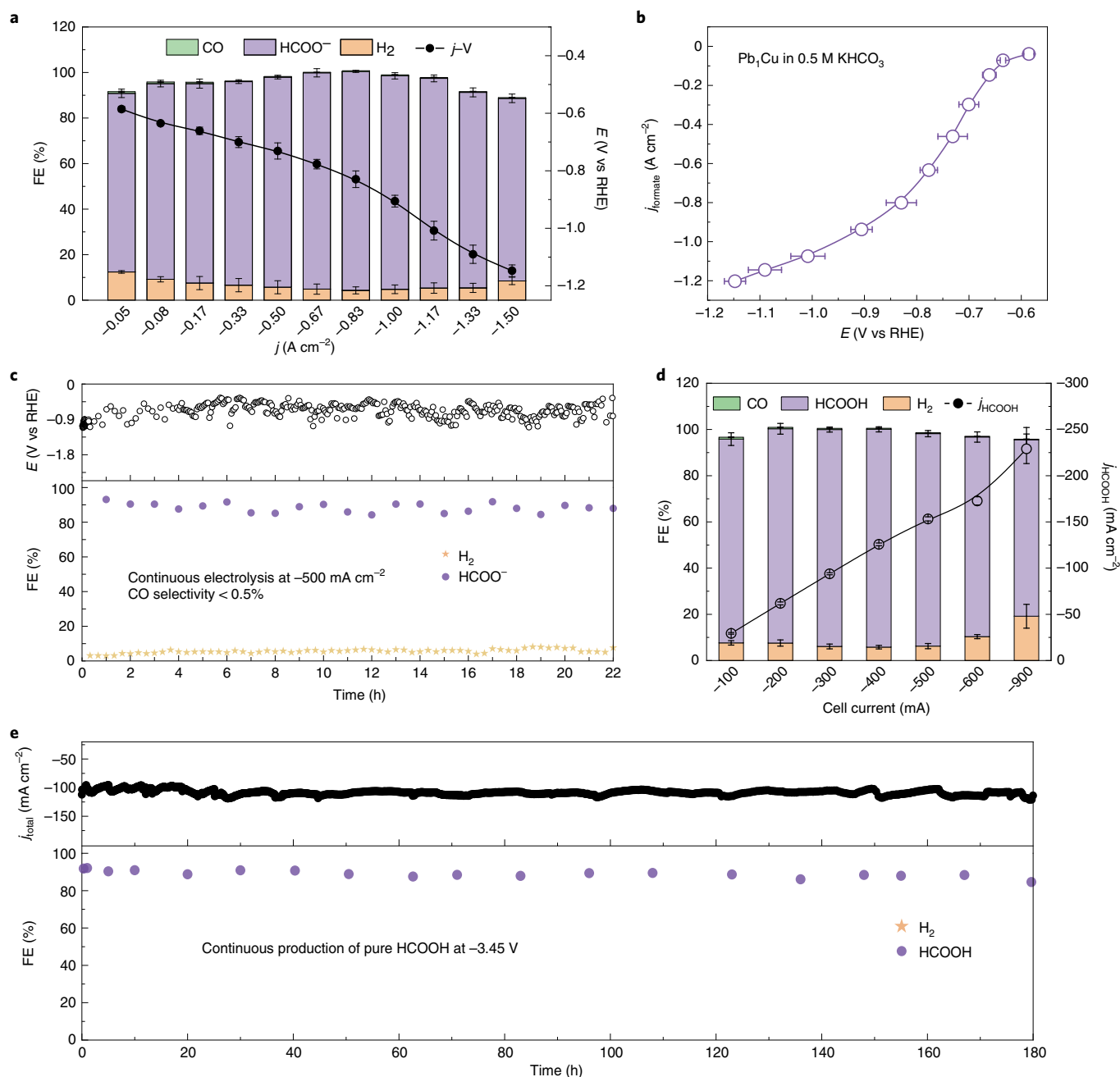


Fig. 2 | CO₂RR performance over in situ formed Pb₁Cu SAAs. **a, FEs of all CO₂RR products at different current densities and the corresponding j -V curve of Pb₁Cu SAAs. **b**, Variation in the formate partial current density against applied potential over Pb₁Cu SAAs. **c**, Stability test at -500 mA cm⁻² current density in a flow cell for over 20 h, indicating an average formate FE of about 90%, estimated by NMR analysis. **d,e**, Direct production of pure liquid fuel over Pb₁Cu SAAs using a CO₂ reduction device with a solid electrolyte²⁸: FEs of all the products under different cell currents, along with the corresponding HCOOH partial current density (**d**), and long-term operation of the reduction device for pure HCOOH solution production at -3.45 V (**e**). The Pb₁Cu catalyst demonstrates an impressive stability over 180 h at an average current density of -100 mA cm⁻² (3 cm² electrode). The HCOOH FE was maintained above -85% during continuous operation for 180 h. The error bars correspond to the standard deviation of three independent measurements.**

a current density of -667 mA cm⁻² (Supplementary Fig. 32). When the current density of Bi₁Cu was ramped up to -1,000 mA cm⁻², the formate FE still remained above 90%, generated along with around 2% CO and 4% H₂. However, the In₁Cu catalyst co-generated CO and formate as major products (Supplementary Fig. 32). The Bi₁Cu and In₁Cu controls demonstrate that the Cu site selectivity for CO₂RR could be regulated using different isolated alloying atoms. Other specific products, such as methanol and methane, might also be exclusively produced on Cu catalysts by appropriate single-atom alloying.

In addition, we conducted density functional theory (DFT) calculations to understand the global activity trend and mechanism of CO₂RR on all the studied SAA catalysts, as well as the exclusive features of the Pb₁Cu case. As discussed previously³⁶, a step surface is more selective for CO₂RR to formic acid. Thus, a set of SAA step (211) surfaces (M₁Cu, M = Pb, In, Bi), as well as the pristine Cu(211) surface, were constructed (Supplementary Fig. 33) to study the CO₂RR activity trend. Two competitive reaction pathways for formic acid production were considered explicitly,

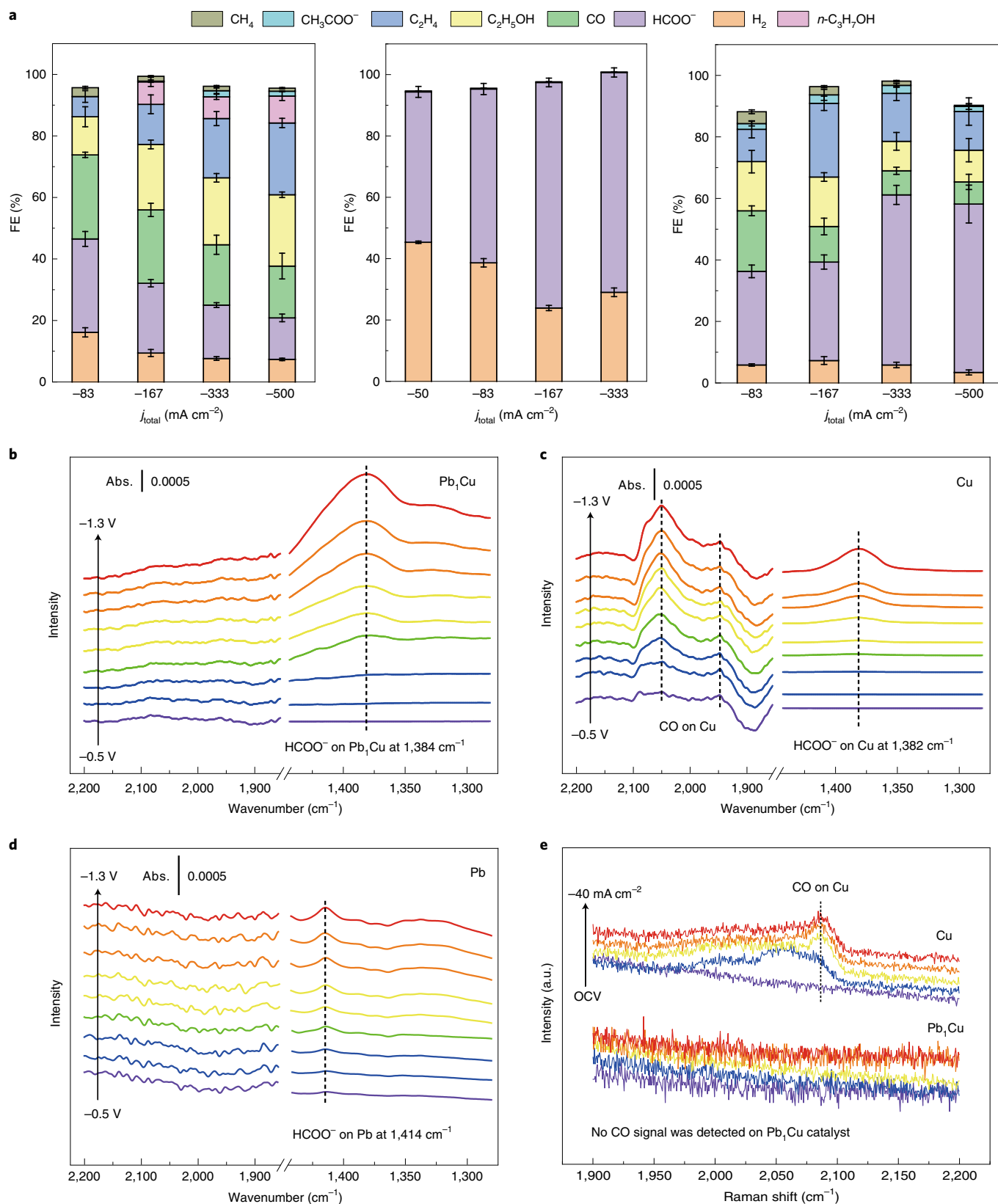


Fig. 3 | Mechanistic studies of the electrochemical CO₂-to-formate conversion on Pb₁Cu. **a, Comparison of product FEs on Cu (left), Pb (centre) and Pb₁Cu (right) nanoparticles. **b–d**, In situ ATR-FTIR spectra recorded at different applied potentials (without *iR* compensation) for the Pb₁Cu SAA (**b**), pure Cu nanoparticles (**c**) and Pb nanoparticles (**d**). Abs., absorbance. **e**, In situ Raman spectra recorded at different current densities for Cu and Pb₁Cu SAA catalysts, showing the absence of CO formation on the Pb₁Cu catalyst. OCV, open-circuit voltage.**

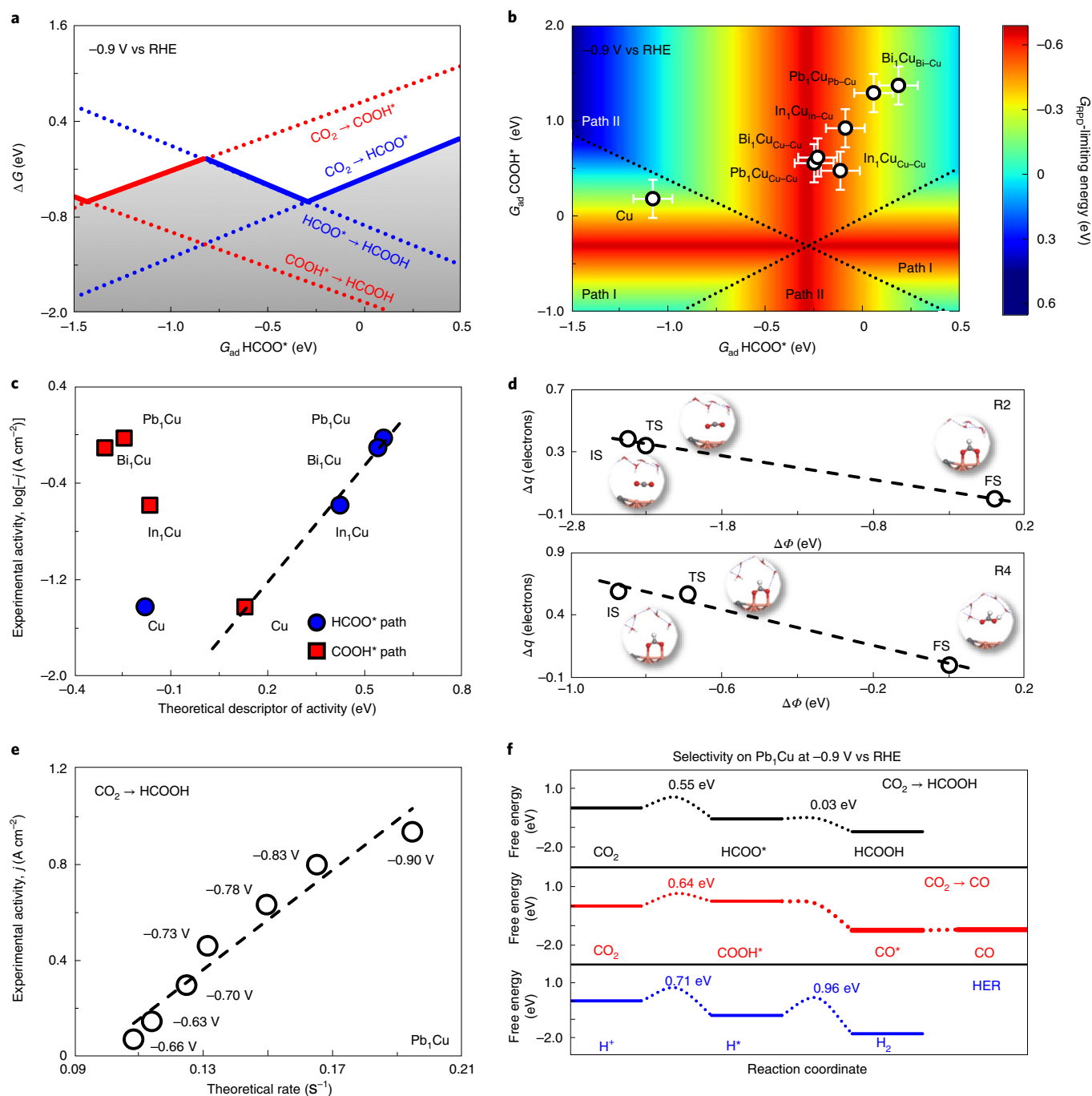
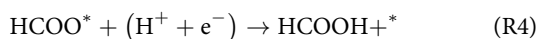
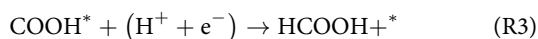
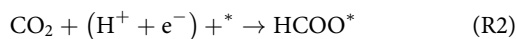
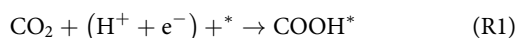


Fig. 4 | Theoretical calculations. **a**, The one-dimensional RPD for CO_2RR . The dotted lines represent the reaction free energy for R1–R4. The solid lines show the G_{RPD} -limiting steps for the more favoured COOH^* path (R1+R3, red lines) and the HCOO^* path (R2+R4, blue lines). **b**, The two-dimensional RPD for CO_2RR producing formate based on two independent descriptors, the adsorption free energies of HCOO^* and COOH^* , on various surfaces considering different adsorption sites (Supplementary Fig. 33). Error bars of 0.1 and 0.2 eV for the HCOO^* and COOH^* adsorption energies, respectively, are considered due to the uncertainty of the solvent effect. The more favoured paths are divided by dotted lines, where path I represents the COOH^* path and path II represents the HCOO^* path. The activity trend is described by the G_{RPD} -limiting energies at the electrode potential of -0.9 V versus RHE. The colour code shows G_{RPD} -limiting energies from -0.6 to 0.6 eV, consistent with Supplementary Fig. 38. **c**, Comparison between the theoretical descriptor of activity ($-G_{\text{RPD}}$ -limiting) and the experimental activity ($\log[-j \text{ (A cm}^{-2}\text{)}]$). The dashed line shows the correlation between experimental and theoretical activity, which is described by the G_{RPD} -limiting energy of the more favoured path through either COOH^* or HCOO^* . **d**, Linear relations between the amount of electrons transferred from the electrode to the water layer (Δq) and the relative work function of the system ($\Delta\Phi$) at the initial (IS), transition (TS) and final (FS) states for R2 and R4 in the HCOO^* mechanism. **e**, Comparison between the theoretically calculated rate from microkinetic simulations and the experimental formate partial current density at various electrode potentials. **f**, Free-energy diagrams for the competition between CO_2RR producing formate or CO and the HER reaction at the electrode potential of -0.9 V versus RHE.

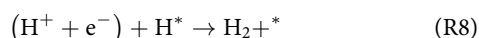
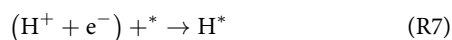
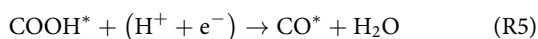
namely, via COOH* (path I: R1 + R3) and via HCOO* (path II: R2 + R4).



The adsorption structures of COOH* and HCOO* on various surfaces and sites are shown in Supplementary Fig. 33. An explicit model shows the solvation stabilizations for COOH* and HCOO* to be 0.18 and 0.06 eV, respectively, which are consistent with the calculations based on implicit models (Supplementary Fig. 34 and Supplementary Tables 5 and 6). According to the correlation between the COOH* and HCOO* adsorption energies (Supplementary Fig. 35), a global activity trend along with relevant mechanisms can be obtained from a thermodynamic perspective by varying the HCOO* adsorption free energies (G_{adHCOO^*}), named the reaction phase diagram (RPD; Fig. 4a). The four bold lines in Fig. 4a represent the globally optimal limiting free energies ($G_{\text{RPD-limiting}}$), accounting for the more favourable path via COOH* for strongly reactive catalysts, whereas the HCOO* path is favoured by catalysts with relatively weak reactivity (see Supplementary Information for a more mechanistic analysis of the RPD). A double-peak activity volcano trend was found due to different mechanisms following either the COOH* or HCOO* path, consistent with previous work^{11,37}.

Towards a more accurate description of the activity trend, a two-dimensional RPD was established (Fig. 4b) on the basis of two independent descriptors (the adsorption free energies of COOH* and HCOO*). The activity trend of formic acid production can be estimated using the $G_{\text{RPD-limiting}}$ energies, which gave strong agreement with the experimental trend of $\text{Pb}_1\text{Cu} > \text{Bi}_1\text{Cu} > \text{In}_1\text{Cu} > \text{Cu}$ (Fig. 4c). Note that the COOH* path is only preferred on Cu(211) (Supplementary Fig. 36). However, the HCOO* path is more favourable with lower $G_{\text{RPD-limiting}}$ energies over all the studied SAA surfaces (M_1Cu , $\text{M} = \text{Pb, In, Bi}$) due to the appropriately weaker HCOO* binding energies compared with on Cu(211), explained well by the *d*-band model (Supplementary Fig. 37a,b). Moreover, the good correlation between the theoretical descriptor of activity and the experimental activity indicates the importance of both paths (Fig. 4c). In addition, the activity on other terrace (100) and (111) surfaces for either the SAAs or pure Pb, Bi and In have also been studied for comparison (Supplementary Figs. 33, 38 and 39). Different active sites on Pb_1Cu were studied as well (Supplementary Fig. 40), which revealed weaker HCOO* binding on the Pb-top site, explained well by the projected density of states between O 2p and Cu or Pb (Supplementary Fig. 37c). In short, the Cu site on the Pb_1Cu step surface shows the highest CO₂RR activity towards exclusive formate production.

Towards understanding the exclusive CO₂RR selectivity for formate in comparison with CO and HER on Pb_1Cu , a few key elementary steps of the HER and CO production were studied for comparison.



The potential-dependent activation barriers were explicitly calculated on the basis of the ‘charge-extrapolation’ scheme^{38,39} within the capacitor model. The strong correlations between the amount of electron transfer from the electrode to the water layer (Δq) and the relative work function of the system ($\Delta\Phi$) at the initial, transition and final states (R2 and R4 are shown as examples in Fig. 4d) again revealed the reliability of the capacitor model in these systems. Therefore, the relative variation in the kinetic barriers is reliable^{40,41}, even though there are dynamic water structures at the electrode interface. As a result, activation barriers were calculated at specific work functions, which can be extrapolated to varying electrode potentials (Supplementary Tables 7 and 8; for details of the ‘charge-extrapolation’ scheme, see Supplementary Information). According to the theoretical microkinetic modelling^{42,43}, the excellent linear correlation between the theoretical reaction rate and experimental partial current density indicates the potential effect can be captured (Fig. 4e).

In addition, the potential-dependent activation barriers for all the electrochemical steps in the CO₂RR and HER were explicitly calculated (Supplementary Fig. 41). The free-energy diagrams for these processes at −0.9 V versus RHE on Pb_1Cu are shown in Fig. 4f. CO₂ protonation to HCOO* exhibits a lower barrier (0.55 eV) than CO₂ protonation to COOH* (0.64 eV). No additional barriers were determined for the protonation of COOH* to CO* (R5) and the desorption of CO* (R6) at −0.9 V versus RHE. Hence, the first protonation determines the high formate selectivity with respect to CO production. Moreover, the Heyrovsky step (R8) has a larger barrier of 0.96 eV (Fig. 4f), resulting in a slow HER. Microkinetic simulations confirmed again the high selectivity for formate on Pb_1Cu (Supplementary Table 9).

Conclusion

Taken together, the experimental and theoretical results described herein showcase a new Cu catalyst design principle for CO₂RR towards formate by mediating the intermediate priority path, suggesting further avenues for engineering Cu catalysts for specific single products. Given the wide variety of single-atom modifiers, our strategy could in principle be extended to generate other value-added pure liquid fuels. Furthermore, we would like to clarify that, due to the lack of in situ technology that can directly observe the intermediate adsorption on a specific site, other possibilities, for example, that both Pb surrounded by Cu and Cu with Pb nearby serve as the active sites, cannot be ruled out completely, and will be thoroughly explored in our future work.

Online content

Any methods, additional references, Nature Research reporting summaries, source data, extended data, supplementary information, acknowledgements, peer review information; details of author contributions and competing interests; and statements of data and code availability are available at <https://doi.org/10.1038/s41565-021-00974-5>.

Received: 17 February 2021; Accepted: 4 August 2021;

Published online: 16 September 2021

References

- Wu, Y., Jiang, Z., Lu, X., Liang, Y. & Wang, H. Domino electroreduction of CO₂ to methanol on a molecular catalyst. *Nature* **575**, 639–642 (2019).
- Wang, X. et al. Efficient electrically powered CO₂-to-ethanol via suppression of deoxygenation. *Nat. Energy* **5**, 478–486 (2020).
- Li, F. et al. Cooperative CO₂-to-ethanol conversion via enriched intermediates at molecule–metal catalyst interfaces. *Nat. Catal.* **3**, 75–82 (2020).
- Morales-Guio, C. G. et al. Improved CO₂ reduction activity towards C₂₊ alcohols on a tandem gold on copper electrocatalyst. *Nat. Catal.* **1**, 764–771 (2018).
- Spurgeon, J. M. & Kumar, B. A comparative technoeconomic analysis of pathways for commercial electrochemical CO₂ reduction to liquid products. *Energy Environ. Sci.* **11**, 1536–1551 (2018).

6. Chen, C., Kotyk, J. F. K. & Sheehan, S. W. Progress toward commercial application of electrochemical carbon dioxide reduction. *Chem* **4**, 2571–2586 (2018).
7. Lu, X., Leung, D. Y., Wang, H., Leung, M. K. & Xuan, J. Electrochemical reduction of carbon dioxide to formic acid. *ChemElectroChem* **1**, 836–849 (2014).
8. Zheng, X. et al. Sulfur-modulated tin sites enable highly selective electrochemical reduction of CO₂ to formate. *Joule* **1**, 794–805 (2017).
9. Zheng, X. et al. Theory-guided Sn/Cu alloying for efficient CO₂ electroreduction at low overpotentials. *Nat. Catal.* **2**, 55–61 (2019).
10. Yang, F. et al. Bismuthene for highly efficient carbon dioxide electroreduction reaction. *Nat. Commun.* **11**, 1088 (2020).
11. Shi, Y. et al. Unveiling hydrocerussite as an electrochemically stable active phase for efficient carbon dioxide electroreduction to formate. *Nat. Commun.* **11**, 3145 (2020).
12. Kang, X. et al. Quantitative electro-reduction of CO₂ to liquid fuel over electro-synthesized metal–organic frameworks. *J. Am. Chem. Soc.* **142**, 17384–17392 (2020).
13. De Arquer, F. P. G. et al. CO₂ electrolysis to multicarbon products at activities greater than 1 A cm⁻². *Science* **367**, 661–666 (2020).
14. Li, C. W., Ciston, J. & Kanan, M. W. Electroreduction of carbon monoxide to liquid fuel on oxide-derived nanocrystalline copper. *Nature* **508**, 504–507 (2014).
15. Lv, J. J. et al. A highly porous copper electrocatalyst for carbon dioxide reduction. *Adv. Mater.* **30**, 1803111 (2018).
16. Arán-Ais, R. M., Scholten, F., Kunze, S., Rizo, R. & Cuenya, B. R. The role of in situ generated morphological motifs and Cu(I) species in C₂₊ product selectivity during CO₂ pulsed electroreduction. *Nat. Energy* **5**, 317–325 (2020).
17. Xu, H. et al. Highly selective electrocatalytic CO₂ reduction to ethanol by metallic clusters dynamically formed from atomically dispersed copper. *Nat. Energy* **5**, 623–632 (2020).
18. Kim, D., Kley, C. S., Li, Y. & Yang, P. Copper nanoparticle ensembles for selective electroreduction of CO₂ to C₂–C₃ products. *Proc. Natl Acad. Sci. USA* **114**, 10560–10565 (2017).
19. Li, J. et al. Electroreduction of CO₂ to formate on a copper-based electrocatalyst at high pressures with high energy conversion efficiency. *J. Am. Chem. Soc.* **142**, 7276–7282 (2020).
20. Tao, Z., Wu, Z., Wu, Y. & Wang, H. Activating copper for electrocatalytic CO₂ reduction to formate via molecular interactions. *ACS Catal.* **10**, 9271–9275 (2020).
21. Birdja, Y. Y. et al. Advances and challenges in understanding the electrocatalytic conversion of carbon dioxide to fuels. *Nat. Energy* **4**, 732–745 (2019).
22. Feaster, J. T. et al. Understanding selectivity for the electrochemical reduction of carbon dioxide to formic acid and carbon monoxide on metal electrodes. *ACS Catal.* **7**, 4822–4827 (2017).
23. Peterson, A. A., Abild-Pedersen, F., Studt, F., Rossmeisl, J. & Nørskov, J. K. How copper catalyzes the electroreduction of carbon dioxide into hydrocarbon fuels. *Energy Environ. Sci.* **3**, 1311–1315 (2010).
24. Montoya, J. H., Shi, C., Chan, K. & Nørskov, J. K. Theoretical insights into a CO dimerization mechanism in CO₂ electroreduction. *J. Phys. Chem. Lett.* **6**, 2032–2037 (2015).
25. Greiner, M. T. et al. Free-atom-like *d* states in single-atom alloy catalysts. *Nat. Chem.* **10**, 1008–1015 (2018).
26. Zhang, X. et al. Platinum–copper single atom alloy catalysts with high performance towards glycerol hydrogenolysis. *Nat. Commun.* **10**, 5812 (2019).
27. Yang, M. et al. Identifying phase-dependent electrochemical stripping performance of FeOOH nanorod: evidence from kinetic simulation and analyte–material interactions. *Small* **16**, 1906830 (2020).
28. Xia, C. et al. Continuous production of pure liquid fuel solutions via electrocatalytic CO₂ reduction using solid-electrolyte devices. *Nat. Energy* **4**, 776–785 (2019).
29. Xia, C., Xia, Y., Zhu, P., Fan, L. & Wang, H. Direct electrosynthesis of pure aqueous H₂O₂ solutions up to 20% by weight using a solid electrolyte. *Science* **366**, 226–231 (2019).
30. Fan, L., Xia, C., Zhu, P., Lu, Y. & Wang, H. Electrochemical CO₂ reduction to high-concentration pure formic acid solutions in an all-solid-state reactor. *Nat. Commun.* **11**, 3633 (2020).
31. Moradzaman, M. & Mul, G. Infrared analysis of interfacial phenomena during electrochemical reduction of CO₂ over polycrystalline copper electrodes. *ACS Catal.* **10**, 8049–8057 (2020).
32. Kim, C. et al. Achieving selective and efficient electrocatalytic activity for CO₂ reduction using immobilized silver nanoparticles. *J. Am. Chem. Soc.* **137**, 13844–13850 (2015).
33. Li, Y. et al. Promoting CO₂ methanation via ligand-stabilized metal oxide clusters as hydrogen-donating motifs. *Nat. Commun.* **11**, 6190 (2020).
34. Kortlever, R., Shen, J., Schouten, K. J. P., Calle-Vallejo, F. & Koper, M. T. Catalysts and reaction pathways for the electrochemical reduction of carbon dioxide. *J. Phys. Chem. Lett.* **6**, 4073–4082 (2015).
35. Hossain, M. N., Wen, J., Konda, S. K., Govindhan, M. & Chen, A. Electrochemical and FTIR spectroscopic study of CO₂ reduction at a nanostructured Cu/reduced graphene oxide thin film. *Electrochem. Commun.* **82**, 16–20 (2017).
36. Ye, K. et al. Synergy effects on Sn–Cu alloy catalyst for efficient CO₂ electroreduction to formate with high mass activity. *Sci. Bull.* **65**, 711–719 (2020).
37. Li, Z. et al. Elucidation of the synergistic effect of dopants and vacancies on promoted selectivity for CO₂ electroreduction to formate. *Adv. Mater.* **33**, 2005113 (2020).
38. Chan, K. & Nørskov, J. K. Potential dependence of electrochemical barriers from ab initio calculations. *J. Phys. Chem. Lett.* **7**, 1686–1690 (2016).
39. Chan, K. & Nørskov, J. K. Electrochemical barriers made simple. *J. Phys. Chem. Lett.* **6**, 2663–2668 (2015).
40. Guo, C., Fu, X. & Xiao, J. Theoretical insights on the synergy and competition between thermochemical and electrochemical steps in oxygen electroreduction. *J. Phys. Chem. C* **124**, 25796–25804 (2020).
41. Li, H., Guo, C., Fu, Q. & Xiao, J. Toward fundamentals of confined electrocatalysis in nanoscale reactors. *J. Phys. Chem. Lett.* **10**, 533–539 (2019).
42. Guo, C., Mao, Y., Yao, Z., Chen, J. & Hu, P. Examination of the key issues in microkinetics: CO oxidation on Rh(1 1 1). *J. Catal.* **379**, 52–59 (2019).
43. Chen, J.-F., Mao, Y., Wang, H.-F. & Hu, P. Reversibility iteration method to understand reaction networks and to solve micro-kinetics in heterogeneous catalysis. *ACS Catal.* **6**, 7078–7087 (2016).

Publisher's note Springer Nature remains neutral with regard to jurisdictional claims in published maps and institutional affiliations.

© The Author(s), under exclusive licence to Springer Nature Limited 2021

Methods

See the Supplementary Information for detailed descriptions of the methods employed in this study.

Chemicals. Copper(II) chloride dihydrate ($\text{CuCl}_2 \cdot 2\text{H}_2\text{O}$), lead nitrate ($\text{Pb}(\text{NO}_3)_2$), bismuth nitrate pentahydrate ($\text{Bi}(\text{NO}_3)_3 \cdot 5\text{H}_2\text{O}$), indium nitrate hydrate ($\text{In}(\text{NO}_3)_3 \cdot 5\text{H}_2\text{O}$), sodium borohydride (NaBH_4), isopropanol (>99.7%), propylene oxide (>99.5%) and ethanol (>99.7%) were purchased from Sinoreagent. All the chemicals were used without further purification.

Materials synthesis. Pb_1Cu SAA catalyst. First, the Cu–Pb precursor was synthesized using an epoxide gelation approach. First, 515 mg $\text{CuCl}_2 \cdot 2\text{H}_2\text{O}$ and 115 mg $\text{Pb}(\text{NO}_3)_2$ were dissolved in 2 ml isopropanol in a vial. Under bath sonication, 2 ml propylene oxide and 0.2 ml H_2O were then successively added, forming a green gel. The green gel was aged for 1 day and dried at 60 °C under vacuum overnight. The Pb_1Cu SAA catalyst was then formed in situ by reducing the Cu–Pb precursor at a constant current density of -500 mA cm^{-2} for 30 min in a standard three-electrode flow cell system supplied with CO_2 gas, with 0.5 M KHCO_3 as electrolyte.

Cu, Pb and Pb@Cu particles. Cu and Pb nanoparticles were synthesized in an approach similar to that used for the Pb_1Cu SAA catalyst, except that 515 mg $\text{CuCl}_2 \cdot 2\text{H}_2\text{O}$ or 500 mg $\text{Pb}(\text{NO}_3)_2$, respectively, was used. To synthesize the Pb@Cu particles, 5 ml of a 10 mM $\text{Pb}(\text{NO}_3)_2$ solution was added to a suspension of 50 mg Cu nanoparticles in 15 ml of H_2O with constant stirring, followed by the dropwise addition of a 50 mM NaBH_4 solution. This reaction was conducted for 1 h.

Bi_1Cu and In_1Cu SAAs. Bi_1Cu and In_1Cu SAAs were synthesized in a similar approach to that used for the Pb_1Cu SAA, except that $\text{Pb}(\text{NO}_3)_2$ was replaced with 170 mg $\text{Bi}(\text{NO}_3)_3 \cdot 5\text{H}_2\text{O}$ or 96 mg $\text{In}(\text{NO}_3)_3 \cdot 5\text{H}_2\text{O}$, respectively.

Electrochemical measurements. All the electrochemical measurements were conducted at room temperature. A CHI electrochemical workstation was employed for the electrochemical measurements. The typical three-electrode cell measurements were performed using a conventional flow cell and a customized gas-tight H-type glass cell. For the study in aqueous electrolyte in the flow cell, precursor inks were air-brushed onto a gas diffusion layer (YLS-30T GDL) as the cathode electrode with a mass loading of $\sim 0.5 \text{ mg cm}^{-2}$. A piece of Ni foam was adopted as the anode for water oxidation. The two electrodes were then placed on opposite sides of two 1-cm-thick polytetrafluoroethylene (PTFE) sheets with $0.4 \text{ cm} \times 1.5 \text{ cm}$ channels such that the catalyst layer interfaced with the flowing electrolyte. The geometric surface area of the catalyst was 0.6 cm^2 . A Nafion 115 film (Fuel Cell Store) was sandwiched between the two PTFE sheets to separate the chambers. On the cathode side, a titanium gas flow chamber supplied $50 \text{ cm}^3 \text{ min}^{-1}$ CO_2 (monitored by an Alicat Scientific mass flow controller). In addition, 0.5 M KHCO_3 was circulated around the anode and cathode at a flow rate of 1.0 ml min^{-1} during the CO_2RR . An Ag/AgCl electrode was used as the reference electrode. For measurements in the H-cell, the Pb_1Cu catalyst was formed in situ in a flow cell and then transferred to the H-cell separated by a Nafion 115 film. All potentials measured against Ag/AgCl in this work were converted to the RHE scale using the expression $E_{\text{RHE}} = E_{\text{Ag/AgCl}} + 0.197 + 0.0591 \times \text{pH}$. Solution resistance (R_s) was determined by potentiostatic electrochemical impedance spectroscopy at frequencies ranging from 0.1 Hz to 200 kHz. All the potentials measured using the three-electrode set-up were manually compensated.

For the two-electrode cells with solid proton conductor for pure HCOOH solution production²⁸, an anion-exchange membrane (Dioxide Materials and Membranes International) and a Nafion film (Fuel Cell Store) were used for anion and cation exchange, respectively. Around 0.5 mg cm^{-2} Pb_1Cu loaded onto the YLS-30T GDL electrode (3.0 cm^2 electrode area) was used as the cathode, and IrO_2 loaded onto a titanium mesh as the anode. The cathode side was supplied with $30 \text{ cm}^3 \text{ min}^{-1}$ humidified CO_2 gas, and 0.5 M H_2SO_4 aqueous solution was circulated around the anode side at 2 ml min^{-1} . Porous styrene-divinylbenzene sulfonated co-polymer was used as the solid ion conductor²⁹. Deionized water at a flow rate

of 0.75 ml min^{-1} was used to release the HCOOH produced within the solid-state electrolyte layer. All the potentials measured using the two-electrode set-up were manually compensated.

CO_2 reduction product analysis. To quantify the gas products obtained during CO_2 electrolysis, pure CO_2 gas was delivered into the cathodic compartment at a constant rate and vented into a gas chromatograph (Shimadzu GC-2014) equipped with a thermal conductivity detector, a Molsieve 5 Å column and a flame ionization detector. The liquid products were quantified by collecting and analysing the electrolyte using a 400 MHz NMR spectrometer. Typically, after electrolysis, $600 \mu\text{l}$ electrolyte was mixed with $100 \mu\text{l}$ D_2O (Sigma Aldrich, 99.9 at. % D) and $0.05 \mu\text{l}$ dimethylsulfoxide (Sigma Aldrich, 99.9%) as internal standard.

Data availability

All data that support the findings of this study are available in the main text, figures and Supplementary Information, or from the corresponding authors upon reasonable request. Source data are provided with this paper.

Acknowledgements

C.X. acknowledges the University of Electronic Science and Technology of China (UESTC) for startup funding (A1098531023601264) and the NSFC (22102018 and 52171201). J.Z. acknowledges the National Key Research and Development Program of China (2019YFA0405600), the National Science Fund for Distinguished Young Scholars (21925204), the NSFC (U19A2015), the Fundamental Research Funds for the Central Universities, the Provincial Key Research and Development Program of Anhui (202004a05020074), the DNL Cooperation Fund, CAS (DNL202003) and the USTC Research Funds of the Double First-Class Initiative (YD2340002002). This work was partially carried out at the USTC Center for Micro and Nanoscale Research and Fabrication. J.X. acknowledges the Ministry of Science and Technology of China (2018YFA0704503), the Strategic Priority Research Program of the Chinese Academy of Sciences (XDB36030200), the NSFC (91845103), the DNL Cooperation Fund, CAS (DNL202003) and the LiaoNing Revitalization Talents Program (XLYC1907099). T.Z. acknowledges the China Postdoctoral Science Foundation (2019TQ0300 and 2020M671890) and the NSFC (22005291). A.L. acknowledges the Beijing Outstanding Young Scientist Program (BJJWZYJH01201914430039). The authors thank Beijing Synchrotron Radiation Facility (beam line BL1W1B) and Taiwan Photon Source (beamline 44A) for providing beam time.

Author contributions

The project was conceptualized by C.X. and J.Z. and supervised by J.Z., C.X. and J.X. T.Z. and C.L. prepared the catalysts and performed the catalytic tests. T.Z., M.Z., Q.J. and W.X. performed the catalyst characterizations. A.L. conducted the HAADF-STEM characterizations. C.G. and J.X. carried out the DFT calculations. C.-W.P. performed the ex situ EXAFS measurements. C.L., X.L. and H.L. carried out the in situ measurements. T.Z., C.X. and J.Z. wrote the paper with the input from all authors. All authors discussed the results and commented on the manuscript.

Competing interests

The authors declare no competing interests.

Additional information

Supplementary information The online version contains supplementary material available at <https://doi.org/10.1038/s41565-021-00974-5>.

Correspondence and requests for materials should be addressed to Jianping Xiao, Chuan Xia or Jie Zeng.

Peer review information *Nature Nanotechnology* thanks Miao Zhong and the other, anonymous, reviewer(s) for their contribution to the peer review of this work.

Reprints and permissions information is available at www.nature.com/reprints.